

# Mechanism of Polyfluorene Interlayer in Ultraviolet Photodetector: Barrier-Blocking Electron Transport and Light-Inducing Hole Injection

Dezhong Zhang,<sup>†</sup> Ruiliang Xu,<sup>†</sup> Liang Sun,<sup>§</sup> Chuan Chen,<sup>§</sup> Fengli Gao,<sup>†</sup> Xindong Zhang,<sup>†</sup> Jingran Zhou,<sup>\*,†</sup> and Shengping Ruan<sup>\*,†,‡</sup>

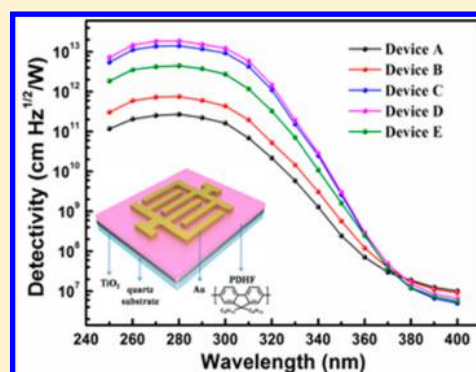
<sup>†</sup>State Key Laboratory on Integrated Optoelectronics and College of Electronic Science & Engineering, Jilin University, Changchun 130012, P. R. China

<sup>‡</sup>State Key Laboratory on Applied Optics, Changchun 130023, P. R. China

<sup>§</sup>Global Energy Interconnection Research Institute, Beijing 102211, P. R. China

## S Supporting Information

**ABSTRACT:** A remarkable performance ultraviolet (UV) photodetector was demonstrated by introducing a poly(9,9-dihexylfluorene) (PDHF) interlayer with the roles of barrier-blocking electron transport and light-inducing hole injection, leading to enhanced properties of the device both in dark and under UV illumination. The PDHF interlayer can efficiently block the electrons, which provides low dark current as well as the reduced noise for devices. Furthermore, the accumulation of photogenerated electrons causes the energy-band bending, leading to promoted gain of holes under UV illumination. The specific detectivity of the device with the PDHF interlayer reaches  $1.86 \times 10^{13} \text{ cm Hz}^{1/2} \text{ W}^{-1}$ . Moreover, the response and recovery speed have been upgraded due to the improvement of the carrier transport mechanism.



## 1. INTRODUCTION

Highly sensitive ultraviolet (UV) photodetectors are needed in wide fields such as light-wave communications, remote control, environmental monitoring, and optoelectronic circuits.<sup>1–5</sup> To date, various wide band gap inorganic semiconductors have been utilized for the matrix materials of UV photodetectors such as  $\text{TiO}_2$ ,  $\text{ZnO}$ ,  $\text{SnO}_2$ , and  $\text{NiO}$ , due to their intrinsic visible-blindness and that they are environmental friendly and thermally and chemically stable.<sup>6–11</sup> Different n-type wide band gap semiconductors have been applied in UV devices, and  $\text{TiO}_2$  drew a lot of attention and extensive investigation for the UV sensing applications,<sup>12–14</sup> especially employed to the device with Schottky metal–semiconductor–metal (MSM) structure,<sup>15–17</sup> which enjoys the positive properties of high working repeatability and low dark current.<sup>18–20</sup> To satisfy the growing demands of high performance photosensing devices, tremendous efforts have been devoted to achieve remarkable devices with low noise, high responsivity, and fast response speed. Yu employed a  $\text{MgO}$  interlayer to modify the  $\text{ZnO}$ -based MSM device, which is attributed to the impact ionization process occurring in the  $\text{MgO}$  insulation layer, obtaining highly improved responsivity.<sup>21,22</sup> As for the  $\text{TiO}_2$  MSM UV photodetector, although the dark current of the device can be limited by the Schottky barrier, there is no efficient way to further reduce the dark current and noise lower, so that the cost-effective MSM structure device is obstructed to be applied to high-precision UV detection. Furthermore, reducing the

noise and improving the gain of the device simultaneously is more difficult, which has become a research focus in UV photodetectors based on MSM structure.

In recent years, conjugated polymers have attracted much attention in science and technology.<sup>23–25</sup> There has been wide interest in the properties of conjugated polymer thin films since the first demonstrations of polymer light emitting film devices. These materials have been used as an active medium in several optoelectronic devices, such as field effect transistors, light emitting diodes, and polymer solar cells.<sup>26–30</sup> The poly(9,9-dihexylfluorene) (PDHF) is one kind of conjugated polymer, which has superior performance of electro-luminescence or single carrier conduction. Typically, the PDHF film is used for hole conduction, which is determined by its energy level position.<sup>31,32</sup> In this study, the polyfluorene film is first applied to the UV photodetector modifying the Schottky contact between the  $\text{TiO}_2$  film and Au electrodes, contributing to improve the device performance both in the dark and under UV illumination. The PDHF interlayer provides a high electron barrier, which avoids the generation of hot electron current; thus, the dark current and noise current can be significantly lowered. While under UV illumination, the PDHF closing to the anode (called A-PDHF) can reduce the hole potential

Received: August 6, 2016

Revised: October 21, 2016

Published: October 31, 2016

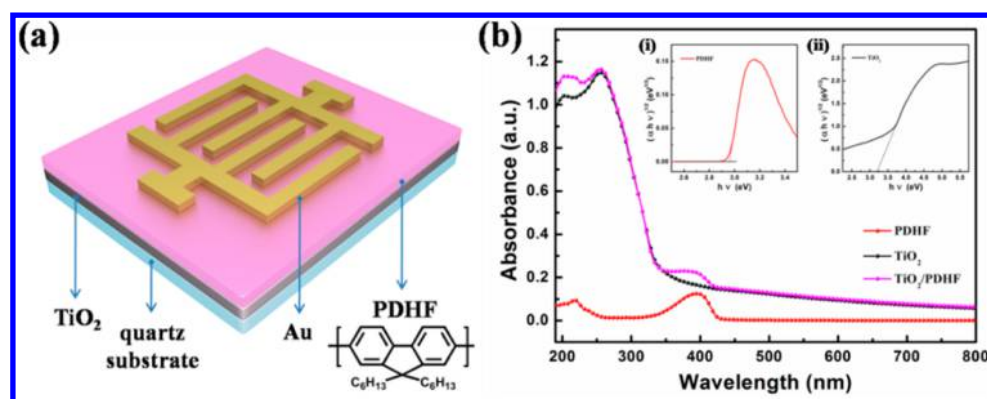


**Figure 1.** (a) Schematic of the UV photodetector with PDHF film. (b) Absorbance spectra of PDHF,  $\text{TiO}_2$ , and  $\text{TiO}_2/\text{PDHF}$ . The insets are the band gap of (i) PDHF film and (ii)  $\text{TiO}_2$  film.

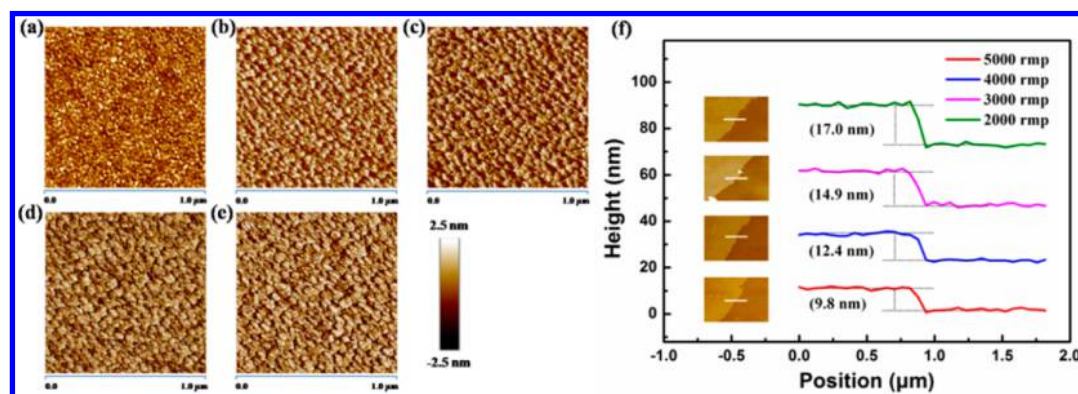


**Figure 2.** AFM images of (a) bare  $\text{TiO}_2$  film and PDHF films with spin speeds of (b) 5000, (c) 4000, (d) 3000, and (e) 2000 rpm. (f) The cross section curves of PDHF films measured by AFM.

barrier and promote the hole injection, connecting to the cathode (called C-PDHF) acts as a hole extraction layer. Accordingly, this UV photodetector with PDHF interlayer represents a remarkable device with ultralow dark current and high gain of holes, as well as improved response and recovery speed.

## 2. EXPERIMENTAL SECTION

$\text{TiO}_2$  was synthesized on a quartz substrate by the sol–gel method, and the detailed preparation process has been provided in our previous reports.<sup>33</sup> The thickness of  $\text{TiO}_2$  film was about 100 nm. PDHF used in this work was commercially available, and it was used without further purification. The PDHF was dissolved in tetrahydrofuran with a concentration of 1000 ppm, then spin-coated on  $\text{TiO}_2$  film at a speed of 5000, 4000, 3000, and 2000 rpm, respectively, followed by thermal annealing at 80 °C for 20 min. Subsequently, the Au interdigitated electrodes were sputtered on PDHF film. Both the finger width and the spacing were 20  $\mu\text{m}$ , and the total effective area was 0.38  $\text{mm}^2$ .

The absorption spectra were measured on a Shimadzu UV-1700 Pharma Spec UV spectrophotometer. The surface morphology was analyzed by a Bruker Dimension Icon Atomic Force Microscope (AFM). The energy levels were investigated by ultraviolet photoelectron spectroscopy (UPS) with He I excitation. The  $I$ – $V$  characteristics and responsivity of devices were measured using a Keithley 2601 source meter together with a UV power meter. A 30 W deuterium lamp was used as the light source, and the monochromatic light was provided by

a monochromator. The noise current was measured by an Advantest R9211C fast Fourier transform (FFT) servo analyzer. The time response characteristics were obtained by an oscilloscope.

## 3. RESULT AND DISCUSSION

We fabricated the devices with a PDHF interlayer, as shown in Figure 1a, and the control device with a bare  $\text{TiO}_2$  layer was also prepared in our experiments, named device A. In this work, PDHF was spin-coated onto  $\text{TiO}_2$  film with different thicknesses, fabricating four kinds of devices with spin speeds of 5000, 4000, 3000, and 2000 rpm, which were named devices B, C, D, and E, respectively. UV light irradiates from the side of quartz. To make a realistic evaluation of the UV selectivity of the  $\text{TiO}_2/\text{PDHF}$  composite film and extract the optical band gaps of  $\text{TiO}_2$ , PDHF, and  $\text{TiO}_2/\text{PDHF}$  films within the wavelength range 190–800 nm, shown in Figure 1b.  $\text{TiO}_2$  film has remarkable absorption at wavelengths of less than 350 nm, closing to the lower edge of the solar-blind region, and the PDHF (3000 rpm) film demonstrates a slight absorption peak at 390 nm. For the  $\text{TiO}_2/\text{PDHF}$  composite film, the absorption edge is consistent with that of pristine  $\text{TiO}_2$  film and valuably enhanced light absorption from 190 to 250 nm can be observed, which exhibits significant UV absorption and the property of solar-blinding. Seen from the inset of Figure 1b, the band gaps of  $\text{TiO}_2$  and PDHF fitted from the  $(ah\nu)^{1/2} - h\nu$ <sup>34</sup> are 3.21 and 2.96 eV, respectively, which are approximate with some previous references.<sup>35,36</sup>

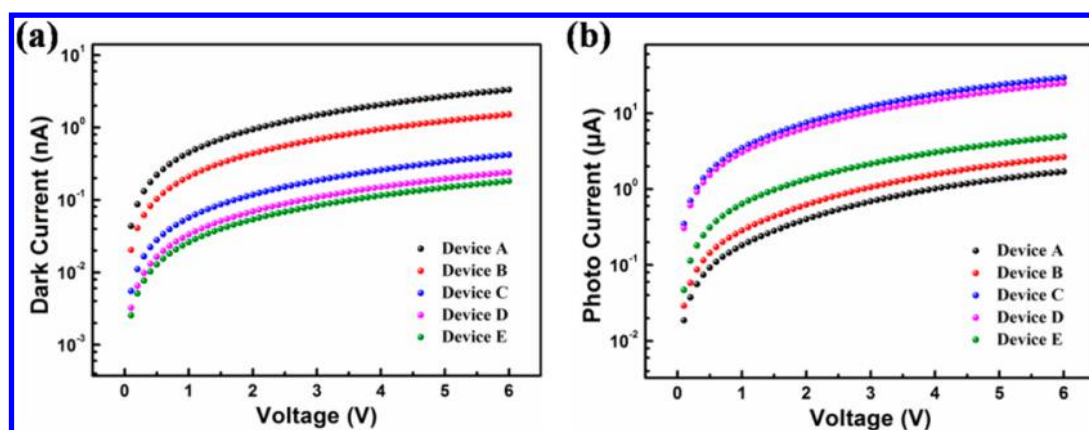


Figure 3.  $I$ – $V$  characteristics of all devices (a) in the dark and (b) under 280 nm UV illumination, measured in the range from 0 to 6 V.

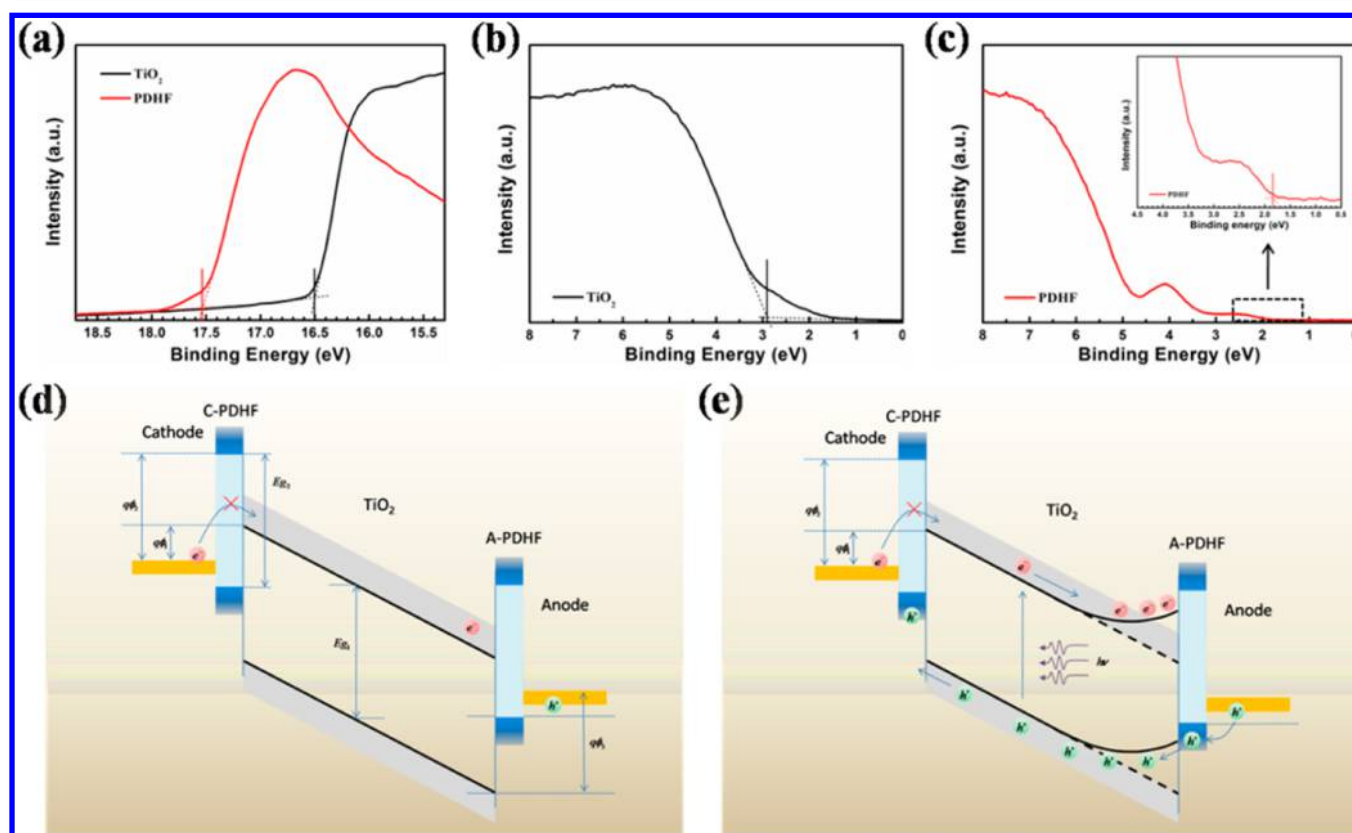


Figure 4. (a–c) The UPS spectra of  $\text{TiO}_2$  and PDHF. The energy level diagrams of the device (d) in the dark and (e) under UV illumination.

The surface morphology and thickness of spin-coated film are crucial factors for the charge transport and recombination, significantly influencing the property of the UV photodetector. Thus, to investigate the morphology of PDHF and characterize the thickness of PDHF under different spin speeds, AFM images were measured for bare  $\text{TiO}_2$  film and PDHF films with different spin speeds, shown in Figure 2a–e, and corresponding cross section curves of PDHF films were exhibited in Figure 2f. The average roughness ( $R_a$ ) can be calculated as the arithmetic average of the absolute values of the surface height deviations, which can be obtained by

$$R_a = \frac{1}{N} \sum_{i=1}^N |\Delta z_i| \quad (1)$$

where  $\Delta z$  is the surface height deviation measured from the mean surface plane and  $N$  is the total number of data points in the scan.<sup>37,38</sup> For the  $\text{TiO}_2$  film,  $R_a$  is 0.579 nm and the  $\text{TiO}_2$  nanoparticles are evenly distributed with a uniform size of 20 nm attained by the magnified SEM image of  $\text{TiO}_2$  film (inset of Figure S2a, Supporting Information), contributing to a good device performance. The  $R_a$  values of PDHF films are 0.720, 0.895, 1.152, and 1.321 nm, suggesting that spin speed will remarkably affect the roughness of the films and lower spin speed is consistent with higher roughness, which can be well proved by the roughness profiles of  $\text{TiO}_2$  film and PDHF films shown in Figure S1 (Supporting Information). To measure the film thickness of different films, some intentional scratch was drawn on the PDHF films to obtain the cross sections and AFM images were measured near the cross section shown in



Figure 2f. It shows that the thickness of PDHF films with spin speeds of 5000, 4000, 3000, and 2000 rpm are 9.8, 12.4, 14.9, and 17.0 nm, respectively. SEM images of TiO<sub>2</sub> film and different PDHF films are shown in Figure S2 (Supporting Information). We can find that TiO<sub>2</sub> film consists of homogeneous particles. PDHF is a continuous film, made up of uniform aggregate structures. With the decrease of the spin-coated speed, film compactness gradually increases. X-ray diffraction (XRD) measurements of TiO<sub>2</sub>/PDHF films cannot give viable information, which is for the reason that the PDHF film is too thin to demonstrate any specific reflection peaks.

To investigate the impact of the PDHF interlayer on the electrical properties, the typical *I*–*V* characteristics of devices A–E in the dark and under UV illumination with a light power of 15  $\mu\text{W cm}^{-2}$  at 280 nm were measured in Figure 3a and b. First, devices B–E exhibit a lower dark current compared with device A without PDHF, and with increased thickness of the PDHF, dark current will reduce sequentially. At 6 V bias, the dark current of device A and device E is 3.32 ( $\pm 0.01$ ) nA and 0.18 ( $\pm 0.01$ ) nA; that of the others is located between these two values. Different from the dark current, the variation tendency of the photocurrent first increases and then decreases with the increase of the PDHF thickness, obtaining the maximum photocurrent for device C. Seen from Figure 3b, the photocurrents at 6 V bias for devices A–E are 1.70, 2.65, 29.34, 24.82, and 4.91  $\mu\text{A}$ , respectively. The effect on the *I*–*V* characteristics of devices due to the incorporation of the PDHF will be analyzed through energy level diagrams in the following discussion.

In order to well explain the work mechanism of PDHF devices, we will investigate the energy levels of TiO<sub>2</sub> and PDHF by UPS, shown in Figure 4a–c. Figure 4a shows the UPS spectra in view of the high binding energy region, which reveal the work function of TiO<sub>2</sub> (4.72 eV) and PDHF (3.70 eV). According to the low binding energy region of the TiO<sub>2</sub> spectrum in Figure 4b, the value of the valence band maximum ( $V_{\text{BM}}$ ) is located at 2.90 eV below the Fermi level. For the PDHF (Figure 4c), the highest occupied states of the  $V_{\text{BM}}$  is located at 1.82 eV lower than the Fermi level. Associating with the optical absorption band gaps got above, energy levels of TiO<sub>2</sub> and PDHF can be attained and then energy level diagrams of device with PDHF interlayer in dark and under illumination could be draw up, shown in Figure 4d and e. In the dark, the barrier located between Au and TiO<sub>2</sub> would increase from  $q\phi_1$  (ca. 0.7 eV) to  $q\phi_2$  (ca. 2.5 eV) due to the existence of the C-PDHF, which will more efficiently block the hot electron injection. At the same time, A-PDHF can also successfully block the electron transport from TiO<sub>2</sub> to the anode. Thus, the dark current of the device with PDHF is reduced compared with the control device due to the limitation of the hot electron current. In addition, with the increase of the PDHF film thickness, the capacity of blocking the electrons will be enhanced, leading to lower dark current, just as the variation tendency of dark current in Figure 3a. Under UV illumination, photogenerated electrons and holes are produced in the TiO<sub>2</sub> layer. PDHF possesses an excellent capacity of hole transport, which contributes to the transfer of photogenerated holes from TiO<sub>2</sub> to the cathode. While photogenerated electrons are prevented by A-PDHF, the transport of photogenerated electrons will be restricted. Therefore, a large number of electrons accumulate in the TiO<sub>2</sub> layer closing to the anode, leading to the energy-band bending, which decreases the hole barrier and thus enhances the hole injection to provide gain of

the photodetector. The PDHF interlayer mainly plays two roles for the enhancement of the device property: one is the barrier-blocking electron transport, and the other is the light-inducing hole injection. With the increase of the thickness of PDHF, the blocking capacity of A-PDHF is gradually improved, but the hole transport ability is decreased by degrees. Thus, at a certain thickness of the PDHF, photocurrent (hole current) achieves the maximum value, perfectly illustrating the reason that device C possesses optimal photocurrent, higher than that of other devices.

In order to prove the photocurrent of the device with PDHF is the hole gain current analyzed above, we did some comparative experiments. On the basis of device D, a TiO<sub>2</sub> layer is prepared by the magnetron sputtering method between the PDHF layer and Au electrodes. The new TiO<sub>2</sub> interlayer in a thickness of ca. 10 nm could transfer electrons and block holes. The schematic of this control device (device D<sub>0</sub>) is shown in inset a of Figure 5. Figure 5 shows the comparison of

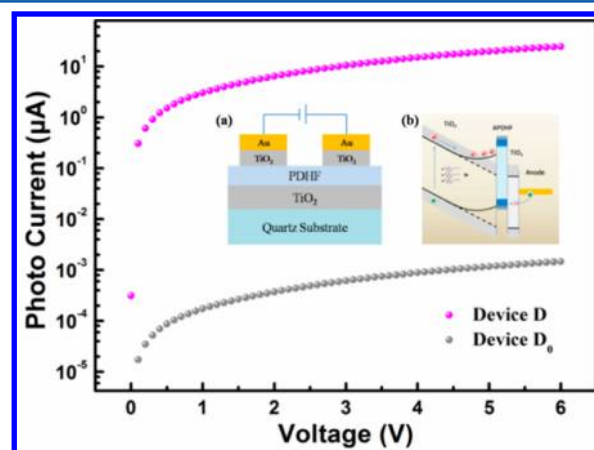


Figure 5. Comparison of the photocurrent between device D and device D<sub>0</sub>. The insets show (a) the schematic and (b) the energy level diagram of device D<sub>0</sub>.

the photocurrent of device D and device D<sub>0</sub> in the same as the previous test conditions. Compared with device D, the photocurrent of device D<sub>0</sub> is significantly decreased by about 4 orders of magnitude. Inset b is the energy level diagram at the anode side of device D<sub>0</sub>. It can be found that the hole injection is blocked due to the high hole barrier. At this time, neither electrons nor holes can be smoothly transferred through the device, leading to significant reduction of the photocurrent.

Figure 6a is the responsivity (*R*) as a function of wavelength from 250 to 400 nm under a bias of 6 V, which can be obtained by

$$R = \frac{I_{\text{ph}}}{P \times S} \quad (2)$$

where  $I_{\text{ph}}$  is the photocurrent (the current directly measured at different wavelengths),  $P$  is the light power density, and  $S$  is the effective area of the device. We can find that the *R* of all devices reaches the peak value at 270 or 280 nm, and the maximum spectral *R* observed is 514.8 A/W at a wavelength of 280 nm for device C. Under the same condition, the value of *R* is determined by the photocurrent. It can be seen from Figure 6a that the devices with PDHF present a higher *R* than that of the control device in the range 250–350 nm, but the *R* values of all devices demonstrate a downward trend surpassing 280 nm due

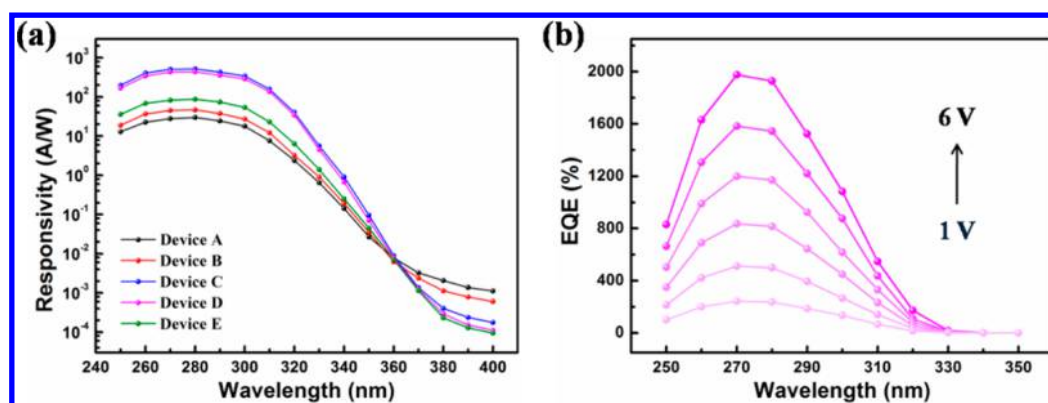


Figure 6. (a) The spectral response characteristics of all devices. (b) The spectral EQE curves of device D under different bias.

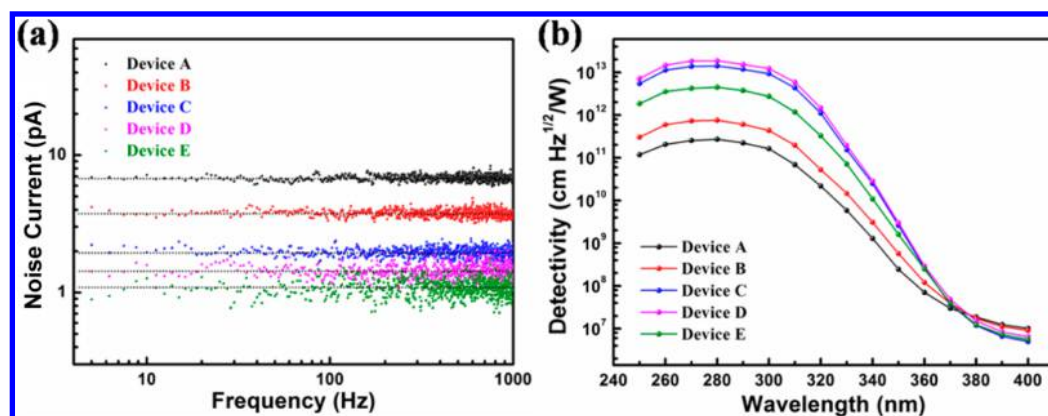


Figure 7. (a) The noise current of devices at 6 V bias with a frequency range from 1 Hz to 1 kHz. (b) The specific detectivity of UV photodetectors at different wavelengths.

to the decreased absorption of the  $\text{TiO}_2$  film. At high wavelength,  $R$  of the devices with PDHF is lower than that of the control device, which can be explained by the fact that, in the range 370–400 nm, the device working state approximated dark conditions; thus,  $R$  depends on the dark current variation. At the same time, the external quantum efficiency (EQE) can be calculated by

$$\text{EQE} = R \times h\nu \quad (3)$$

where  $h\nu$  is the energy of the incident photon in electronvolts. Figure 6b shows the EQE spectra from 250 to 350 nm of device D under different biases (1–6 V). At a bias of 6 V, the peak value of the EQE exceeds 1900%. Though the value of EQE reduces with the decrease of the applied bias, it is still higher than 100% when the bias is 1 V, suggesting that the hole gain exists in a low bias operating condition.

Noise current seriously affects the photodetector property; thus, the total noise currents ( $I_n$ ) of all devices were measured within a frequency range from 1 Hz to 1 kHz, shown in Figure 7a. The tested results suggested that noise currents obtained from all devices act as white noise, which consists of shot noise and some other possible noise, such as flicker noise and thermal noise. Compared with others, the shot noise dominates the main white noise.<sup>39,40</sup> The devices with PDHF possess a lower noise than that of device A, and it continuously decreases with the increase of the PDHF thickness. This is because the total noise current characteristics of all devices are dominated by the shot noise, and the shot noise limit is given by the following<sup>41</sup>

$$i_n^{1/2} = \sqrt{2eI_d\Delta f} \quad (4)$$

where  $i_n^{1/2}$  is the shot noise limit,  $e$  is the electron charge,  $I_d$  is the dark current of the device, and  $\Delta f$  is the frequency internal over which the noise is measured. Thus, the variation of noise current is similar to that of the dark current. Moreover, the specific detectivity ( $D^*$ ) of the UV photodetector is given by the following<sup>42</sup>

$$D^* = \frac{(A\Delta f)^{1/2}R}{I_n} \quad (5)$$

where  $A$  is the effective area of the device and  $R$  is the responsivity.  $D^*$  can be calculated at different wavelengths with the measured  $I_n$  and  $R$  at 6 V bias. The comparison of spectral  $D^*$  from 250 to 400 nm is shown in Figure 7b. Device D has the highest  $D^*$  in the UV region from 250 to 320 nm, and the peak value reaches  $1.86 \times 10^{13} \text{ cm Hz}^{1/2} \text{ W}^{-1}$  at 280 nm.

Time response characteristics are important for the high quality UV photodetector; therefore, the time response was also measured for devices A and D shown in Figure 8. Usually, the response and recovery time of the MSM UV photodetector vary in the range of seconds to tens of seconds.<sup>43–45</sup> However, in our study, for device A, the raise time (from 10 to 90% of the peak value) and the decay time (from 90 to 10% of the peak value) are 638 ms and 2.92 s, and the device with PDHF exhibits a quicker response and recovery speed of 417 ms and 1.37 s for the raise and decay time. The enhanced time response characteristics due to the inset of the PDHF interlayer

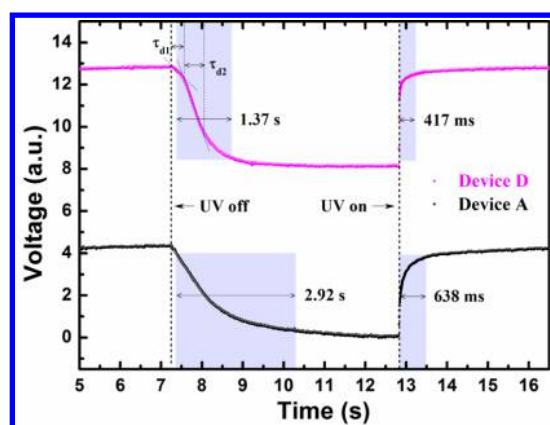


**Figure 8.** Comparison of time response characteristics between devices A and D.

will be attributed to the changed carrier transport mechanism. It can be obviously noted that the decay time of device D can be divided into two parts including  $\tau_{d1}$  and  $\tau_{d2}$  compared with the control device, depicted in Figure 8. We deduce that  $\tau_{d1}$  and  $\tau_{d2}$  correspond to two stages of the device working process: the  $\tau_{d1}$  stage arises from the recombination of excess carriers accumulating near the anode and recovery of the hole barrier height after the UV illumination switching off, which is a softly decaying process. The  $\tau_{d2}$  stage is attributed to the restriction of the hole injection from the anode, as well as the hole extraction by the cathode, causing a sharp reduction of the decay time. Moreover, contrary to the  $\tau_{d1}$  stage, the photogeneration of carriers is relatively fast, leading to the formation of hole gain in a short time after UV switching on. Thus, the improved carrier transport mechanism plays a vital role in improving the response and recovery speed.

#### 4. CONCLUSION

In summary, a high performance UV photodetector has been constructed on the basis of the MSM structure. PDHF film is employed to modify the Schottky contact between  $\text{TiO}_2$  film and Au electrodes, leading to improved performance of the device both in dark and under UV illumination. Due to the high electron barrier provided by the PDHF layer, the dark current and noise current have been significantly reduced. Moreover, the photogenerated electrons can also be limited in  $\text{TiO}_2$  by PDHF, thus resulting in the energy-band bending, which contributes to the gain of holes and the enhanced photocurrent. The specific detectivity of device D reaches  $1.86 \times 10^{13} \text{ cm Hz}^{1/2} \text{ W}^{-1}$ . Owing to the change of the carrier transport mechanism, the response and recovery speed of the device with PDHF has been increased, further improving the performance of the UV photodetector.

#### ■ ASSOCIATED CONTENT

##### Supporting Information

The Supporting Information is available free of charge on the ACS Publications website at DOI: 10.1021/acs.jpcc.6b07956.

Roughness profiles and SEM images  $\text{TiO}_2$  and PDHF films (PDF)

#### ■ AUTHOR INFORMATION

##### Corresponding Authors

\*E-mail: zhoujr@jlu.edu.cn. Phone: +86 431 85168241-8221. Fax: +86 431 85168270.

\*E-mail: ruansp@jlu.edu.cn. Phone: +86 431 85168241-8221. Fax: +86 431 85168270.

##### Notes

The authors declare no competing financial interest.

#### ■ ACKNOWLEDGMENTS

This work was supported by the National Natural Science Foundation of China (Grant Nos. 61274068, 11574110, 61204055, 61404058), Project of Science and Technology Plan of Changchun City (Grant No. 14KG020), Project of Science and Technology Development Plan of Jilin Province (Grant No. 20160204013GX), and Jilin Province Economic Structure Strategic Adjustment Special Plan (2014Y086).

#### ■ REFERENCES

- (1) Lin, Z. H.; Cheng, G.; Yang, Y.; Zhou, Y. S.; Lee, S.; Wang, Z. L. Triboelectric Nanogenerator as an Active UV Photodetector. *Adv. Funct. Mater.* **2014**, *24*, 2810–2816.
- (2) Lu, J. F.; Xu, C. X.; Dai, J.; Li, J. T.; Wang, Y. Y.; Lin, Y.; Li, P. L. Improved UV photoresponse of ZnO Nanorod Arrays by Resonant Coupling with Surface Plasmons of Al Nanoparticles. *Nanoscale* **2015**, *7*, 3396–3403.
- (3) Ni, P. N.; Shan, C. X.; Wang, S. P.; Li, B. H.; Zhang, Z. Z.; Zhao, D. X.; Liu, L.; Shen, D. Z. Enhanced Responsivity of Highly Spectrum-Selective Ultraviolet Photodetectors. *J. Phys. Chem. C* **2012**, *116*, 1350–1353.
- (4) Chen, H. Y.; Liu, K. W.; Hu, L. F.; Al-Ghamdi, A. A.; Fang, X. S. New Concept Ultraviolet Photodetectors. *Mater. Today* **2015**, *18*, 493–502.
- (5) Zhai, T.; Fang, X.; Liao, M.; Xu, X.; Li, L.; Liu, B.; Koide, Y.; Ma, Y.; Yao, J.; Bando, Y.; Golberg, D. Fabrication of High-Quality  $\text{In}_2\text{Se}_3$  Nanowire Arrays toward High-Performance Visible-Light Photodetectors. *ACS Nano* **2010**, *4*, 1596–1602.
- (6) Han, Y. G.; Fan, C. C.; Wu, G.; Chen, H. Z.; Wang, M. Low-Temperature Solution Processed Ultraviolet Photodetector Based on an Ordered  $\text{TiO}_2$  Nanorod Array–Polymer Hybrid. *J. Phys. Chem. C* **2011**, *115*, 13438–13445.
- (7) Peng, S. M.; Su, Y. K.; Ji, L. W.; Wu, C. Z.; Cheng, W. B.; Chao, W. C. ZnO Nanobridge Array UV Photodetectors. *J. Phys. Chem. C* **2010**, *114*, 3204–3208.
- (8) Lee, W. S.; Park, Y. S.; Cho, Y. K. Hierarchically Structured Suspended  $\text{TiO}_2$  Nanofibers for Use in UV and pH Sensor Devices. *ACS Appl. Mater. Interfaces* **2014**, *6*, 12189–12195.
- (9) Zhu, H.; Shan, C. X.; Yao, B.; Li, B. H.; Zhang, J. Y.; Zhao, D. X.; Shen, D. Z.; Fan, X. W. High Spectrum Selectivity Ultraviolet Photodetector Fabricated from an n-ZnO/p-GaN Heterojunction. *J. Phys. Chem. C* **2008**, *112*, 20546–20548.
- (10) Li, X. D.; Gao, C. T.; Duan, H. G.; Lu, B. G.; Wang, Y. Q.; Chen, L. L.; Zhang, Z. X.; Pan, X. J.; Xie, E. Q. High-Performance Photoelectrochemical-Type Self-Powered UV Photodetector Using Epitaxial  $\text{TiO}_2/\text{SnO}_2$  Branched Heterojunction Nanostructure. *Small* **2013**, *9*, 2005–2011.
- (11) Echresh, A.; Chey, C. O.; Shoushtari, M. Z.; Khranovskyy, V.; Nur, O.; Willander, M. UV Photo-Detector Based on p-NiO Thin Film/n-ZnO Nanorods Heterojunction Prepared by a Simple Process. *J. Alloys Compd.* **2015**, *632*, 165–171.
- (12) Xie, Y.; Wei, L.; Li, Q.; Chen, Y.; Yan, S.; Jiao, J.; Liu, G.; Mei, L. High-Performance Self-Powered UV Photodetectors Based on  $\text{TiO}_2$  Nano-branched Arrays. *Nanotechnology* **2014**, *25*, 075202.
- (13) Hou, X. J.; Wang, X. F.; Liu, B.; Wang, Q. F.; Wang, Z. R.; Chen, D.; Shen, G. Z.  $\text{SnO}_2/\text{TiO}_2$  Heterojunction Nanostructures for



Lithium-Ion Batteries and Self-Powered UV Photodetectors with Improved Performances. *ChemElectroChem* **2014**, *1*, 108–115.

(14) Zhang, H.; Ruan, S.; Li, H.; Zhang, M.; Lv, K.; Feng, C.; Chen, W. Schottky Diode Ultraviolet Detector Based on Nanowire Array. *IEEE Electron Device Lett.* **2012**, *33*, 83–85.

(15) Liu, H. Y.; Sun, W. C.; Wei, S. Y.; Yu, S. M. Characterization of TiO<sub>2</sub>-Based MISIM Ultraviolet Photodetectors by Ultrasonic Spray Pyrolysis. *IEEE Photonics Technol. Lett.* **2016**, *28*, 637–640.

(16) Gu, X.; Meng, F.; Liu, G.; Zhang, H.; Zhou, J.; Ruan, S. Influences of Surface Capping with Electrostatically Self-Assembled PEI on the Photoresponse of a TiO<sub>2</sub> Thin Film. *Chem. Commun.* **2013**, *49*, 6328–6330.

(17) Huang, H. L.; Xie, Y. N.; Zhang, Z. F.; Zhang, F.; Xu, Q.; Wu, Z. Y. Growth and Fabrication of Sputtered TiO<sub>2</sub> Based Ultraviolet Detectors. *Appl. Surf. Sci.* **2014**, *293*, 248–254.

(18) He, Y.; Zhang, W.; Zhang, S.; Kang, X.; Peng, W.; Xu, Y. Study of the Photoconductive ZnO UV Detector Based on the Electrically Floated Nanowire Array. *Sens. Actuators, A* **2012**, *181*, 6–12.

(19) Xing, J.; Wei, H.; Guo, E.-J.; Yang, F. Highly Sensitive Fast-Response UV Photodetectors Based on Epitaxial TiO<sub>2</sub> Films. *J. Phys. D: Appl. Phys.* **2011**, *44*, 375104.

(20) Gedamu, D.; Paulowicz, I.; Kaps, S.; Lupan, O.; Wille, S.; Haidarschin, G.; Mishra, Y. K.; Adelung, R. Rapid Fabrication Technique for Interpenetrated ZnO Nanotetrapod Networks for Fast UV Sensors. *Adv. Mater.* **2014**, *26*, 1541–1550.

(21) Yu, J.; Shan, C. X.; Huang, X. M.; Zhang, X. W.; Wang, S. P.; Shen, D. Z. ZnO-Based Ultraviolet Avalanche Photodetectors. *J. Phys. D: Appl. Phys.* **2013**, *46*, 305105.

(22) Yu, J.; Shan, C. X.; Qiao, Q.; Xie, X. H.; Wang, S. P.; Zhang, Z. Z.; Shen, D. Z. Enhanced Responsivity of Photodetectors Realized via Impact Ionization. *Sensors* **2012**, *12*, 1280–1287.

(23) Noriega, R.; Rivnay, J.; Vandewal, K.; Koch, F. P. V.; Stingelin, N.; Smith, P.; Toney, M. F.; Salleo, A. A General Relationship between Disorder, Aggregation and Charge Transport in Conjugated Polymers. *Nat. Mater.* **2013**, *12*, 1038–1044.

(24) Cui, C. H.; Wong, W. Y.; Li, Y. F. Improvement of Open-Circuit Voltage and Photovoltaic Properties of 2D-Conjugated Polymers by Alkylthio Substitution. *Energy Environ. Sci.* **2014**, *7*, 2276–2284.

(25) Mei, J. G.; Bao, Z. N. Side Chain Engineering in Solution-Processable Conjugated Polymers. *Chem. Mater.* **2014**, *26*, 604–615.

(26) Li, W. W.; Roelofs, W. S. C.; Turbiez, M.; Wienk, M. M.; Janssen, R. A. J. Polymer Solar Cells with Diketopyrrolopyrrole Conjugated Polymers as the Electron Donor and Electron Acceptor. *Adv. Mater.* **2014**, *26*, 3304–3309.

(27) Kulkarni, A. P.; Tonzola, C. J.; Babel, A.; Jenekhe, S. A. Electron Transport Materials for Organic Light-Emitting Diodes. *Chem. Mater.* **2004**, *16*, 4556–4573.

(28) Chen, M. X.; Crispin, X.; Perzon, E.; Andersson, M. R.; Pullerits, T.; Andersson, M.; Inganäs, O.; Berggren, M. High Carrier Mobility in Low Band Gap Polymer-Based Field-Effect Transistors. *Appl. Phys. Lett.* **2005**, *87*, No. 252105.

(29) Hu, Z. C.; Zhang, K.; Huang, F.; Cao, Y. Water/Alcohol Soluble Conjugated Polymers for the Interface Engineering of Highly Efficient Polymer Light-Emitting Diodes and Polymer Solar Cells. *Chem. Commun.* **2015**, *51*, 5572–5585.

(30) Zhou, H. X.; Yang, L. Q.; You, W. Rational Design of High Performance Conjugated Polymers for Organic Solar Cells. *Macromolecules* **2012**, *45*, 607–632.

(31) Yoshida, M.; Fujii, A.; Ohmori, Y.; Yoshino, K. Three-Layered Multicolor Organic Electroluminescent Device. *Appl. Phys. Lett.* **1996**, *69*, 734.

(32) Li, H.-G.; Wu, G.; Shi, M. M.; Yang, L. G.; Chen, H. Z.; Wang, M. ZnO/Poly (9, 9-dihexylfluorene) Based Inorganic/Organic Hybrid Ultraviolet Photodetector. *Appl. Phys. Lett.* **2008**, *93*, 153309.

(33) Zhang, M.; Gu, X.; Lv, K.; Dong, W.; Ruan, S.; Chen, Y.; Zhang, H. High Response Solar-Blind Ultraviolet Photodetector Based on Zr<sub>0.5</sub>Ti<sub>0.5</sub>O<sub>2</sub> Film. *Appl. Surf. Sci.* **2013**, *268*, 312–316.

(34) Butler, M. A. Photoelectrolysis and Physical Properties of the Semiconducting Electrode WO<sub>2</sub>. *J. Appl. Phys.* **1977**, *48*, 1914–1920.

(35) Ibnaouf, K. H.; Prasad, S.; Masilamani, V.; AlSalhi, M. S. Evidence for Amplified Spontaneous Emission from Double Excimer of Conjugated Polymer (PDHF) in a Liquid Solution. *Polymer* **2013**, *54*, 2401–2405.

(36) Yu, W. L.; Cao, Y.; Pei, J.; Huang, W.; Heeger, A. J. Blue Polymer Light-Emitting Diodes from Poly (9, 9-dihexylfluorene-alt-co-2, 5-didecyloxy-para-phenylene). *Appl. Phys. Lett.* **1999**, *75*, 3270–3272.

(37) Doganov, R. A.; O'Farrell, E. C. T.; Koenig, S. P.; Yeo, Y.; Ziletti, A.; Carvalho, A.; Campbell, D. K.; Coker, D. F.; Watanabe, K.; Taniguchi, T.; et al. Accessing the Transport Properties of Pristine Few-Layer Black Phosphorus by van der Waals Passivation in Inert Atmosphere. *Nat. Commun.* **2015**, *6*, 6647.

(38) Tak, Y. H.; Kim, K. B.; Park, H. G.; Lee, K. H.; Lee, J. R. Criteria for ITO (indium–tin-oxide) Thin Film as the Bottom Electrode of an Organic Light Emitting Diode. *Thin Solid Films* **2002**, *411*, 12–16.

(39) Guo, F.; Yang, B.; Yuan, Y.; Xiao, Z.; Dong, Q.; Bi, Y.; Huang, J. A Nanocomposite Ultraviolet Photodetector Based on Interfacial Trap-Controlled Charge Injection. *Nat. Nanotechnol.* **2012**, *7*, 798–802.

(40) Wei, H. T.; Fang, Y. J.; Yuan, Y. B.; Shen, L.; Huang, J. S. Trap Engineering of CdTe Nanoparticle for High Gain, Fast Response, and Low Noise P3HT:CdTe Nanocomposite Photodetectors. *Adv. Mater.* **2015**, *27*, 4975–4981.

(41) Harris, N. C.; Baehr-Jones, T.; Lim, A. E.-J.; Liow, T.; Lo, G.; Hochberg, M. Noise Characterization of a Waveguide-Coupled MSM Photodetector Exceeding Unity Quantum Efficiency. *J. Lightwave Technol.* **2013**, *31*, 23–27.

(42) Gong, X.; Tong, M.; Xia, Y.; Cai, W.; Moon, J. S.; Cao, Y.; Yu, G.; Shieh, C.-L.; Nilsson, B.; Heeger, A. J. High-Detectivity Polymer Photodetectors with Spectral Response from 300 to 1450 nm. *Science* **2009**, *325*, 1665–1667.

(43) Guo, L.; Zhang, H.; Zhao, D. X.; Li, B. H.; Zhang, Z. Z.; Jiang, M. M.; Shen, D. Z. High Responsivity ZnO Nanowires Based UV Detector Fabricated by the Dielectrophoresis Method. *Sens. Actuators, B* **2012**, *166*, 12–16.

(44) Wang, R. C.; Lin, Y. X.; Wu, J. J. Intrinsic n- and p-Type MgZnO Nanorods for Deep-UV Detection and Room-Temperature Gas Sensing. *J. Phys. Chem. C* **2015**, *119*, 29186–29192.

(45) Li, J. Y.; Chang, S. P.; Lin, H. H.; Chang, S. J. High Responsivity Mg<sub>0.9</sub>Zn<sub>0.1</sub>O Film UV Photodetector Grown by RF Sputtering. *IEEE Photonics Technol. Lett.* **2015**, *27*, 978–981.